



HAL
open science

Spectral energy scaling in precessing turbulence

A. Khlifi, A. Salhi, S. Nasraoui, F. Godeferd, C. Cambon

► **To cite this version:**

A. Khlifi, A. Salhi, S. Nasraoui, F. Godeferd, C. Cambon. Spectral energy scaling in precessing turbulence. *Physical Review E*, 2018, 98, 10.1103/PhysRevE.98.011102. hal-02906457

HAL Id: hal-02906457

<https://hal.science/hal-02906457>

Submitted on 24 Jul 2020

HAL is a multi-disciplinary open access archive for the deposit and dissemination of scientific research documents, whether they are published or not. The documents may come from teaching and research institutions in France or abroad, or from public or private research centers.

L'archive ouverte pluridisciplinaire **HAL**, est destinée au dépôt et à la diffusion de documents scientifiques de niveau recherche, publiés ou non, émanant des établissements d'enseignement et de recherche français ou étrangers, des laboratoires publics ou privés.

Spectral energy scaling in precessing turbulence

A. Khlifi,¹ A. Salhi,^{1,2} S. Nasraoui,¹ F. Godefert,² and C. Cambon²¹*Département de Physique, Faculté des sciences de Tunis, 1060 Tunis, Tunisia*²*Laboratoire de Mécanique des Fluides et d'Acoustique, UMR 5509, Université de Lyon, CNRS, ECL, UCBL, INSA, Ecully, France*

(Received 16 January 2018; published 25 July 2018)

We study precessing turbulence, which appears in several geophysical and astrophysical systems, by direct numerical simulations of homogeneous turbulence where precessional instability is triggered due to the imposed background flow. We show that the time development of kinetic energy \mathcal{K} occurs in two main phases associated with different flow topologies: (i) an exponential growth characterizing three-dimensional turbulence dynamics and (ii) nonlinear saturation during which \mathcal{K} remains almost time independent, the flow becoming quasi-two-dimensional. The latter stage, wherein the development of \mathcal{K} remains insensitive to the initial state, shares an important common feature with other quasi-two-dimensional rotating flows such as rotating Rayleigh-Bénard convection, or the large atmospheric scales: in the plane $k_{\parallel} = 0$, i.e., the plane associated to an infinite wavelength in the direction parallel to the principal rotation axis, the kinetic energy spectrum scales as k_{\perp}^{-3} . We show that this power law is observed for wave numbers ranging between the Zeman “precessional” and “rotational” scales, k_S^{-1} and k_{Ω}^{-1} , respectively, at which the associated background shear or inertial timescales are equal to the eddy turnover time. In addition, an inverse cascade develops for $(k_{\perp}, k) < k_S$, and the spherically averaged kinetic energy spectrum exhibits a k^{-2} inertial scaling for $k_S < k < k_{\Omega}$.

DOI: [10.1103/PhysRevE.98.011102](https://doi.org/10.1103/PhysRevE.98.011102)

Introduction. Rotating flows are omnipresent in several geophysical and astrophysical systems. Inertial waves occurring in these flows are generally affected by external boundary conditions and/or by external forces or torques, leading to the apparition of local inertial instabilities. A more complex situation is that of precession where there is a continuous change of the orientation of the rotation axis of the system. In a precessing container, the flow is therefore the result of the complex interplay between inertial waves, Ekman boundary layers, and the base flow [1]. It can eventually become unstable and create space-filling turbulence [2]. In the geophysical context, the turbulent flow driven by precession in the Earth’s outer core is able to feed huge amounts of energy (orders of magnitude can be estimated between 10^{11} and 10^{21} W) and therefore possibly sustain the geomagnetic field [2,3]. In the astrophysical context, precession may trigger instabilities leading to the formation of vortex tangles and generate turbulence in superfluid neutron star interiors [4].

The generic feature of precessional flows appears to be the shearing of streamlines as shown in the independent studies by Kerswell [5] and by Mahalov [6]. Kerswell considers the so-called Poincaré solution [7] characterizing the response of an inviscid fluid within a precessing, oblate spheroid. Mahalov’s uses a different approach, by considering an infinite cylinder in which a tilted (sheared) streamline solution can exist under precession. In both systems, the parametric precessional instability [5,6] arises through a subharmonic resonance between inertial modes and the basic state, with a mechanism similar to that of the elliptical instability [8,9].

The nonlinear evolution of precessional instabilities has been addressed in several experimental, numerical, and theoretical studies exhibiting very rich dynamics, ranging from

laminar flows to fully developed turbulence for both cylindrical geometries [1, 10–12] and spherical or spheroidal ones [13, 14]. An alternative geometry is used by Mason and Kerswell [15] who consider a viscous and incompressible fluid in a plane layer (with rigid stress-free top and bottom boundaries) that spins about its normal which itself precesses about an axis fixed in space. They showed that the flow solution switches chaotically between different nonlinear states over long times and concluded that this phenomenon, which is seemingly unrelated to the fast precessional frequency, is important for the precessing Earth. Recently, in the astrophysical context, Barker [16] considered the simple model by Mason and Kerswell [15] in an unbounded domain and showed that nonlinear interactions which saturate the precessional instability generate turbulence with columnar vortices. This is also found in turbulence subjected to rapid rotation [17]. In rapidly rotating turbulence, the emergence of large-scale vortices characterizes a quasi-two-dimensional (2D) state perpendicular to the fixed rotation axis [18], and, at increasing rotation rate, energy accumulates in the vicinity of the so-called “spectral buffer layer” around $k_{\parallel} \simeq 0$ [17, 19] (k_{\parallel} is the wave-vector component along the rotation axis). At $k_{\parallel} = 0$, inertial waves vanish altogether because their dispersion relation vanishes as well. The separation between the dynamics of velocity modes with nonzero and zero inertial wave frequencies, or equivalently, with $k_{\parallel} \neq 0$ (wave modes) and $k_{\parallel} = 0$ (vortex modes) was discussed and observed in previous studies of rotating flows [20–23]. When the system rotation is coupled with another linear effect, such as buoyancy in rotating Rayleigh-Bénard convection [24, 25], the original version of the Taylor-Proudman theorem, linear and steady, is sufficient to explain the two-dimensionalization. Otherwise, the fact that the 2D motion is dominant in the nonlinear

dynamics of *purely* rotating turbulence is controversial in the sense that inertial wave turbulence theory predicts only partial two-dimensionalization without inverse energy cascade, since the 2D mode is seen as an integrable singularity in an infinite three-dimensional (3D) spatial domain. Confinement, either explicit due to solid boundaries [26], or implicit, due to box periodicity in direct numerical simulations (DNS), can indeed trigger a large-scale inverse cascade.

Our objective here is to provide answers to the following questions, through the analysis of the time evolution of second-order velocity correlations and the development of energy spectra: (i) How does the precessional instability operate in an initially isotropic homogeneous turbulence? (ii) How does the resulting precessing turbulence compare with turbulence driven by precessional instability [16], or with rapidly rotating turbulence, or with rotating turbulence under a ‘‘precession-like’’ perturbation [27]?

Model and equations. In order to address quantitatively these questions important for modeling geophysical and astrophysical flow dynamics, we perform direct numerical simulations of initially isotropic turbulence subjected to the mean flow with mean velocity \mathbf{U} , viewed in the precessing frame rotating uniformly at $\mathbf{\Omega}_p = \varepsilon \mathbf{\Omega} \mathbf{e}_1$. With

$$\mathbf{U}(\mathbf{x}) = \mathbf{M} \cdot \mathbf{x}, \quad \mathbf{M} = \Omega \begin{pmatrix} 0 & -1 & 0 \\ 1 & 0 & 0 \\ 0 & -2\varepsilon & 0 \end{pmatrix}. \quad (1)$$

and $\mathbf{x} = (x_1, x_2, x_3)^T$ the physical coordinate. Equation (1) shows that the mean flow is the superposition of a solid body rotation with a vorticity vector $2\Omega \mathbf{e}_3$ and a linear shear with a vorticity vector $-2\varepsilon \Omega \mathbf{e}_1$ that balances the gyroscopic torque created by the misalignment of $\mathbf{\Omega}$ and $\mathbf{\Omega}_p$ (see schematic on Fig. 2) [29]. This ensures consistency with statistical homogeneity. The Poincaré number $\varepsilon > 0$ controls the degree of nonlinearity of the precessing flow [28]. The mean flow (1) is obtained by transforming the so-called Mahalov’s solution [6,30] into Cartesian coordinates. It expresses the generic precessional response of a fluid, and is realized in the interior of precessing containers where boundary layers typically set the boundary conditions [5].

The Navier-Stokes equations for the fluctuating velocity field $\mathbf{u}(\mathbf{x}, t)$ in the precessing frame are

$$\begin{aligned} \partial_t \mathbf{u} + (\mathbf{U} \cdot \nabla) \mathbf{u} + (\mathbf{u} \cdot \nabla) \mathbf{u} + \mathbf{M} \cdot \mathbf{u} + 2\mathbf{\Omega}_p \times \mathbf{u} \\ = -\nabla p + \nu \nabla^2 \mathbf{u}, \end{aligned} \quad (2)$$

where $\mathbf{u}(\mathbf{x}, t)$ is divergence free, $\nabla \cdot \mathbf{u} = 0$, ν is the kinematic viscosity, and p is the fluctuating pressure divided by the fluid density. Under the assumption that the turbulence is statistically homogeneous, the resulting equation for the turbulent kinetic energy per unit mass $\mathcal{K} = \frac{1}{2} \langle u_i u_i \rangle$, where $\langle \cdot \rangle$ denotes ensemble (statistical) averaging, takes the form $\dot{\mathcal{K}} = \mathcal{P} - \mathcal{D}$, where $\mathcal{P} = 2\varepsilon \Omega \langle u_2 u_3 \rangle$ is the turbulent energy production due to the mean shear (rotation produces no energy), and $\mathcal{D} = \nu \langle \partial_{x_j} u_i \partial_{x_j} u_i \rangle$ is the turbulent dissipation rate per unit mass. An important parameter is the microscale Rossby number [19] $\text{Ro}_\omega = \sqrt{\mathcal{D}}/\nu/(2\Omega)$ which is interpreted as the ratio of the convective to the Coriolis acceleration at the Taylor scale. We represent the fluctuating fields as the superposition of plane

waves using Fourier transforms

$$[\mathbf{u}(\mathbf{x}, t), p(\mathbf{x}, t)] = \int_{\mathbb{R}^3} [\hat{\mathbf{u}}(\mathbf{k}, t), \hat{p}(\mathbf{k}, t)] \exp i[\mathbf{k}(t) \cdot \mathbf{x}] d^3 \mathbf{k},$$

where $\mathbf{k}(t)$ is the time-dependent wave vector. In order to remove the explicit dependence on \mathbf{x} in the resulting equations for the spectral velocity component $\hat{\mathbf{u}}(\mathbf{k}, t)$, one has to ensure that $\mathbf{k}(t)$ varies in time according to $\dot{\mathbf{k}} = -\mathbf{M}^T \cdot \mathbf{k}$. This amounts to following characteristic lines of the mean flows, although expressed in spectral variables (details in Ref. [29]). The spectral equation becomes

$$\dot{\hat{\mathbf{u}}} + \mathbf{M} \cdot \hat{\mathbf{u}} + 2\mathbf{\Omega}_p \times \hat{\mathbf{u}} + i \hat{p}^{(\ell)} \mathbf{k} + \nu k^2 \hat{\mathbf{u}} = -\mathbf{P} \cdot (\widehat{\boldsymbol{\omega}} \times \hat{\mathbf{u}}), \quad (3)$$

with $\mathbf{k} \cdot \hat{\mathbf{u}} = 0$ for the solenoidal velocity field. $\hat{p}^{(\ell)}$ is the spectral counterpart of the linear part of pressure fluctuations, $\boldsymbol{\omega} = \nabla \times \mathbf{u}$ is the vorticity, $P_{ij} = k^{-2} k_j k_i - \delta_{ij}$ is the projection operator where $k = \|\mathbf{k}\|$ is the wave-vector modulus, and δ_{ij} is the Kronecker tensor. Accordingly, the wave-vector components evolve as

$$k_1(t) + 2\varepsilon k_3(t) = (k_{10} + 2\varepsilon k_{30}) \cos(\Omega t) - k_{20} \sin(\Omega t), \quad (4)$$

$$k_2(t) = (k_{10} + 2\varepsilon k_{30}) \sin(\Omega t) + k_{20} \cos(\Omega t), \quad (5)$$

$$k_3(t) = k_{\parallel} = k_{30}, \quad (6)$$

where $\mathbf{k}_0 = (k_{10}, k_{20}, k_{30})^T$ is the initial wave vector. Therefore, the wave-vector trajectories are circles with sheared centers, as their counterparts in physical space, since $\mathbf{k} \cdot \mathbf{x} = \mathbf{k}_0 \cdot \mathbf{x}_0$ [5,15].

Linear solution. In the inviscid linear limit, the stability problem is governed by a two-dimensional linear Floquet system or, equivalently, by Hill’s equation which, at $\varepsilon = 0$, reduces to the inertial waves equation with dispersion relation $\omega_R = \pm 2\mathbf{\Omega} \cdot \mathbf{k}_0/k_0 = \pm 2\Omega k_{\parallel}/k_0$. At $\varepsilon \ll 1$, we apply the perturbation theory [31] to analyze the stability of Hill’s equation and we show that the subharmonic resonant modes are those for which $2\omega_R = \pm \Omega$, so that $k_{\parallel}/k_0 = \pm 1/4$, and at order ε^1 , the maximal growth rate of the precessional shearing instability is $\sigma_m/\varepsilon = 5\sqrt{15}/32 \approx 0.605$ [5,29]. At $k_{\parallel} = 0$, the inviscid linear solution indicates that there is no linear instability: the inertial frequency ω_R is zero and the vertical mode \hat{u}_3 remains identical to its initial value, as it is in the pure rotating case ($\varepsilon = 0$), while the horizontal mode $\hat{u}_2 = -(k_1/k_2)\hat{u}_1$ undergoes a precessing motion with period Ω induced by the vertical mode.

2D nonlinear coupling. Obviously, at $k_{\parallel} = 0$, the nonlinear interactions can generate a coupling between vertical and horizontal modes as shown by the equation for the horizontal and vertical spectral densities of energy, $e_h = \frac{1}{2} \langle |\hat{u}_1|^2 + |\hat{u}_2|^2 \rangle$ and $e_v = \frac{1}{2} \langle |\hat{u}_3|^2 \rangle$,

$$\dot{e}_v^{(2D)} + 2\nu k_{\perp}^2 e_v^{(2D)} = T_v^{(2D)}, \quad (7)$$

$$\dot{e}_h^{(2D)} + 2\nu k_{\perp}^2 e_h^{(2D)} = \pi^{(2D)} + T_h^{(2D)}, \quad (8)$$

in which the superscript (2D) refers to the $k_{\parallel} = 0$ mode. For instance, $e_v^{(2D)}(\mathbf{k}_{\perp}, t) = e_v(\mathbf{k}, t) \delta(\mathbf{k} - \mathbf{k}_{\perp})$ where $\delta(\mathbf{k} - \mathbf{k}_{\perp})$ is the Dirac function, in agreement with the decomposition into two disjoint sets for the wave vector by [32]. $\pi = 2\varepsilon \Omega \Re \langle \hat{u}_2 \hat{u}_3^* \rangle$ denotes the spectral density of production due to mean shear

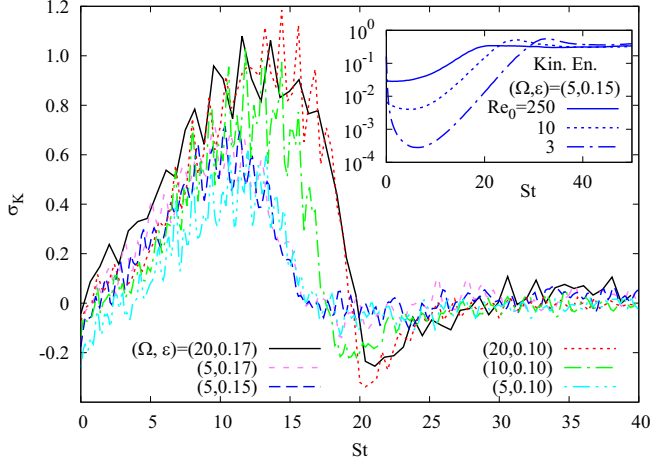


FIG. 1. Time evolution of the kinetic energy growth rate $\sigma_K = (SK)^{-1}\dot{K} = (SK)^{-1}(\mathcal{P} - \mathcal{D})$ for several values of the couple (Ω, ε) . At the saturation stage, σ_K slightly fluctuates about zero reflecting a balance between \mathcal{P} and \mathcal{D} . The inset shows the independence of the saturated kinetic energy to the initial Reynolds number Re_0 .

and T_h, T_v , and $T = T_h + T_v$ are transferlike terms which involve triple velocity correlations such that $\int_{\mathbb{R}^3} T dk = 0$. Our present DNS results indicate that $\int_{\mathbb{R}^2} T_v^{(2D)}(\mathbf{k}_\perp, t) dk_1 dk_2$ is not zero, as in the pure rotating case ($\varepsilon = 0$).

Direct numerical simulations. We solve the fully nonlinear equations of motion (3) by DNS using a modified version of the Fourier spectral code Snoopy developed by [33]. The simulations start from isotropic conditions obtained by a preliminary simulation started with a random initial velocity field with energy spectrum $E(k_0) \propto k_0^4 \exp(-k_0^2/k_p^2)$, where k_p^{-1} is a specified length scale. The initial total kinetic energy is $\mathcal{K}(0) = \int_0^\infty E(k_0) dk_0$. The isotropic precomputation is done *before* applying the mean flow (1) at $t = 0$. During this initial stage only, a large-scale forcing (at $1 \leq k_0 \leq 4$) is applied until a statistical steady state of classical isotropic turbulence is reached, giving a Taylor-microscale-based Reynolds number $Re_\lambda \approx 40$. Additional simulations starting from decaying isotropic turbulence with low Reynolds number $Re_0 = \mathcal{K}_0^2/(vD_0)$ or from a solenoidal random noise for the initial velocity [16] were also performed in order to assess the effects of the initial conditions on the saturation stage of the precessing turbulence (see below). We also limit the effects of L_0 -periodic boundary conditions, by computing all integral scales

$$L_{jj}^{(\ell)} = \frac{1}{\langle u_j u_j \rangle} \int_0^\infty \langle u_j(\mathbf{x}) u_j(\mathbf{x} + r\mathbf{e}_\ell) \rangle dr \quad (9)$$

in the x_ℓ ($\ell = 1, 2, 3$) directions, and imposing that $\max L_{jj}^{(\ell)} \leq 0.25L_0$ (no sum over subscript j). By this, we control numerical confinement, even if one integral length scale grows faster due to precessional instability. Hence, the final dimensionless time $St = 2\varepsilon\Omega t$ appears to be $St = 40$ for all the runs. Aliasing errors are removed using the 2/3 dealiasing rule and the minimum and maximum wave numbers are $k_{\min} = 1$ and $k_{\max} = N/3$. Our DNS resolution is $N = 256$ or $N = 512$ in each Cartesian coordinate direction. The runs were performed for six values of the pair $(\Omega, \varepsilon) = (5, 0.1), (5, 0.15), (5, 0.17), (10, 0.1), (20, 0.1), (20, 0.17)$.

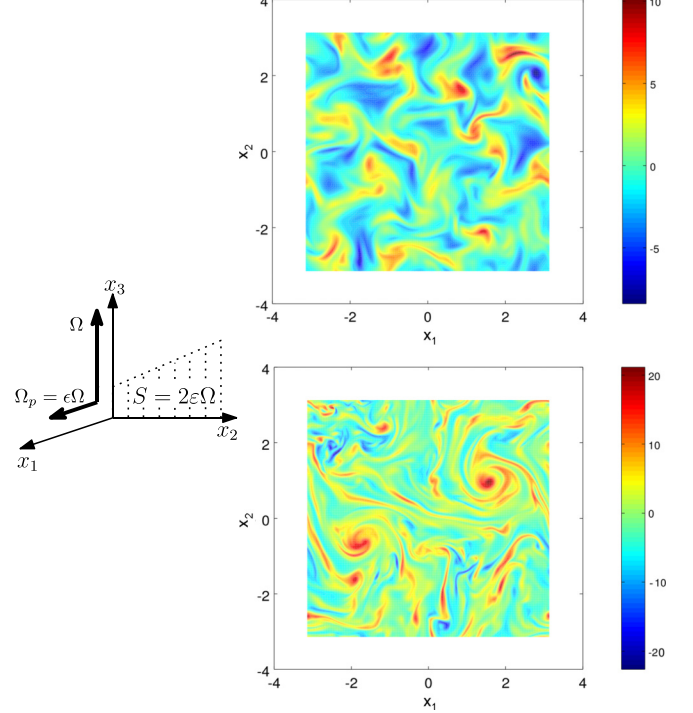


FIG. 2. Left: Schematic of the mean flow. Right: Horizontal cut of vertical vorticity ω_z in the case $(\Omega = 5, \varepsilon = 0.17)$ with resolution 512^3 . In the exponential growth stage (top snapshot at $St = 10$ and $Ro_\omega = 0.25$) one observes large-scale filaments together with intense localized dominant vortices (with highest value of 10), while at the saturation stage (bottom snapshot at $St = 40, Ro_\omega = 0.45$), which corresponds to a quasi-2D flow, there are two large columnar vortices (with highest value of 20) emerging from the background of 3D turbulent fluctuations.

Results of DNS. Our simulations show that there are two important stages characterizing the behavior of the mean turbulent kinetic energy: (i) An initial exponential growth of $\mathcal{K}(t)$ followed by (ii) a saturation stage at $St > 20$, during which $\mathcal{K}(t)$ remains almost constant. This is also clear when observing the evolution of the growth rate $\sigma_K = (SK)^{-1}\dot{K} = (SK)^{-1}(\mathcal{P} - \mathcal{D})$ which slightly fluctuates about zero during the saturation stage (see Fig. 1). At the exponential growth stage, both the mean dissipation rate \mathcal{D} and the production term \mathcal{P} also exhibit an exponential evolution, while at the saturation stage, they decay with time and become slowly balanced such that $\mathcal{P} \sim \mathcal{D}$. Due to the decay of the dissipation rate, the microscale Rossby number Ro_ω also decays during the saturation stage. Its final value (at $St = 40$) ranges between 0.12 and 1.0 depending on the parameters (Ω, ε) . Note that rotating turbulent dynamics with Rossby number $\mathcal{O}(1)$ is typical of geophysical flows [17].

In the following, we analyze the dynamics of the saturation stage and comment about the exponential growth stage when relevant. The kinetic energy level at saturation increases as ε or Ω increases (not plotted), but, at a fixed value of the pair (Ω, ε) , it remains insensitive to the initial Reynolds number [$Re_0 = \mathcal{K}_0^2/(vD_0) \leq 250$], independently of the initial conditions (precomputed initial isotropic or solenoidal random noise) (see the inset of Fig. 1). At the saturation stage, the major contribution to kinetic energy \mathcal{K} comes from the horizontal

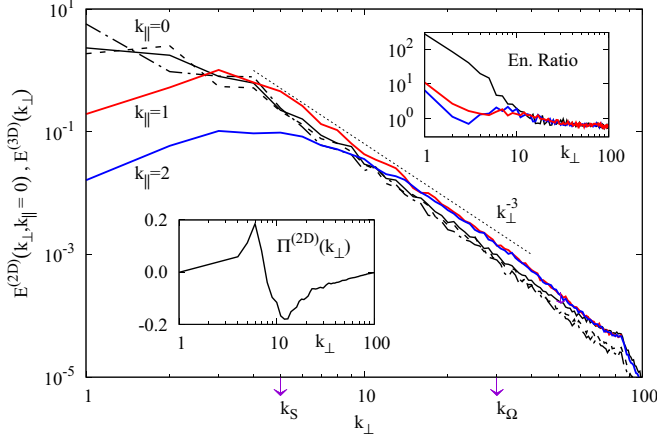


FIG. 3. Energy spectrum $E^{(2D)}(k_{\perp}, k_{\parallel} = 0)$ 2D modes and $E^{(3D)}(k_{\perp})$ of 3D modes $k_{\parallel} = 1, 2$ at the saturation stage for $(\Omega = 20, \varepsilon = 0.17)$, with resolution 512^3 . (The tiny peak at $k = 85$ is a remnant of the precomputation at coarser resolution 256^3 ; it does not affect our current conclusions.) Solid lines for spectra averaged over $St \in [20, 40]$. One observes that the averaged $\langle E^{(2D)}(k_{\perp}) \rangle_t$ and $E^{(2D)}(k_{\perp}, t)$ at $St = 30$ (dashed line) and $St = 40$ (dots) are almost the same, exhibiting a k_{\perp}^{-3} scaling in the range $k_S \sim 5 < k_{\perp} < k_{\Omega} \sim 30$. At large horizontal scales ($k_{\perp} < k_S$), the energy is mainly concentrated around the plane $k_{\parallel} = 0$, and transferred via an inverse cascade that creates a strong anisotropy, as shown by the top inset displaying the energy ratio $E_h^{(2D)}/E_v^{(2D)}$ (dashed) and $E_h^{(3D)}/E_v^{(3D)}$ for $k_{\parallel} = 1, 2$. The bottom inset shows the flux spectrum indicative of backscatter at large scale.

energy \mathcal{K}_h as shown by the right inset of Fig. 4 displaying the evolution of the ratio $\mathcal{K}_h/\mathcal{K}_v$ for $(\Omega = 5, \varepsilon = 0.17)$. This attests to the importance of large-scale anisotropy. Note that the dominance of the horizontal motion over the vertical one is more pronounced in the dynamics of the $k_{\parallel} = 0$ mode than in that of modes with $k_{\parallel} \neq 0$. This is shown by the evolution of the ratio $L_h^{(3)}/L_v^{(3)}$ which grows faster than $\mathcal{K}_h/\mathcal{K}_v$ (see the right inset of Fig. 4), and by noticing that

$$L_{jj}^{(3)} = \langle u_j u_j \rangle^{-1} 2\pi \int_{\mathbb{R}^2} \langle u_j^{(2D)} u_j^{(2D)} \rangle dk_1 dk_2. \quad (10)$$

At the saturation stage, \mathcal{K}_v and $L_v^{(3)}$ decay with time while their horizontal counterparts, \mathcal{K}_h and $L_h^{(3)}$ remain almost constant (not shown). Note that $\langle u_1 u_1 \rangle$ and $\langle u_2 u_2 \rangle$ (respectively, $L_{11}^{(3)}$ and $L_{22}^{(3)}$) exhibit similar behaviors but are not identical, while in the pure rotating case at $\varepsilon = 0$, $\langle u_1 u_1 \rangle = \langle u_2 u_2 \rangle$ and $L_{11}^{(3)} = L_{22}^{(3)}$ due to axisymmetry. The dominance of the horizontal motion in the saturation stage is indicative of a quasi-2D state of turbulence that is characterized by the presence of columnar structures along the solid body rotation, as also proven in visualizations of the vertical vorticity field (see Fig. 2). This quasi-two-dimensional three-component (2D-3C) behavior of the flow at the saturation stage can also be characterized by examining energy spectra (see below). In contrast, in the exponential growth stage, the horizontal motion does not dominate the vertical one. This trend is indicative of a 3D state of the turbulence at this stage.

In Fig. 3 we show the development of the 2D energy spectrum $E^{(2D)}(k_{\perp}, t) = k_{\perp} \int_0^{2\pi} e^{(2D)}(\mathbf{k}_{\perp}, t) d\varphi$ (where $\tan \varphi =$

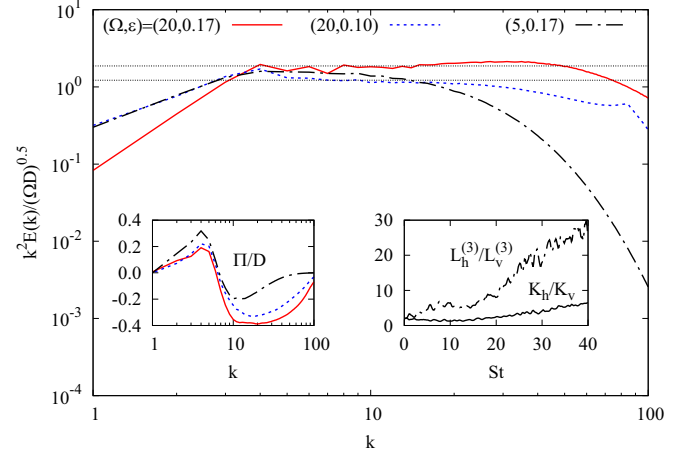


FIG. 4. Average over $St \in [20, 40]$ of the radial spectrum $E(k, t)$ normalized by rotation scaling for $(\Omega, \varepsilon) = (20, 0.17)$, $(20, 0.10)$, and $(5, 0.17)$ with resolutions 512^3 , 256^3 , and 512^3 . Dashed horizontal lines at $C_{\Omega} = 1.22$ and $C_{\Omega} = 1.87$ for reference [see Eq. (11)]. The left inset shows the nonlinear transfer flux normalized by the dissipation rate for the three precessing turbulence cases. Inverse cascade of energy develops at $k < k_S$. The right inset displays the time evolution of the ratio of horizontal energy (respectively, integral length scale associated to $k_{\parallel} = 0$ mode) to vertical energy (respectively, integral length scale) for $(\Omega = 5, \varepsilon = 0.17)$

k_{\perp}/k_{\parallel}), at $St = 30, 40$ and its average $\langle E^{(2D)} \rangle_t(k_{\perp})$ over the time window $St \in [20, 40]$ corresponding to the saturation stage (see Fig. 1). The figure shows that there are no noticeable differences between $E^{(2D)}(k_{\perp}, t)$ and its average $\langle E^{(2D)} \rangle_t(k_{\perp})$ that follows a k_{\perp}^{-3} scaling for $k_S < k_{\perp} < k_{\Omega}$, i.e., for wave numbers very weakly affected by rotation since they are larger than the Zeman scale $k_{\Omega} = (\Omega^3/D)^{1/2} \sim 30$, but more significantly by shear since they are larger than the Corrsin scale $k_S = [(2\varepsilon\Omega^3/D)^{1/2}] \sim 5$ [34, 35]. For $k_{\perp} < k_S$, the major contribution to the 2D total energy $E^{(2D)}(k_{\perp})$ comes from the horizontal part $E_h^{(2D)}$, whereas for $k_{\perp} > k_S$, there is no significant dominance of horizontal or vertical energy, as shown by the top inset of Fig. 3. Even if the dynamics of the spectral buffer layer around $k_{\parallel} = 0$ [17] may not be completely captured by simulations due to discretization between the planes $k_{\parallel} = 0$ and $k_{\parallel} = 1$, similarities between the dynamics of this spectral buffer layer and the dynamics of its near-neighbor 3D modes can be drawn. Thus, as shown by Fig. 3, the spectrum $E^{(3D)}(k_{\perp}) = k_{\perp} \int_0^{2\pi} e(\mathbf{k}, t) d\varphi$ over the planes $k_{\parallel} = 1$ and $k_{\parallel} = 2$, that characterizes the dynamics of the 3D modes also exhibits the spectral scaling k_{\perp}^{-3} . When moving from the plane $k_{\parallel} = 0$ to the plane $k_{\parallel} = 1$ (as well as from the plane $k_{\parallel} = 1$ to the plane $k_{\parallel} = 2$), the large horizontal scales become less energetic and the k_{\perp} range over which the k_{\perp}^{-3} scaling occurs is reduced. In the steeper k_{\perp}^{-3} slope, 3D modes release a significant amount of energy to 2D modes [36–38]. We note that in the exponential growth stage, with respect to spectra in the saturation phase, the spectrum $E^{(2D)}(k_{\perp})$ is shallower for $k_{\perp} < k_S$ but is steeper than k_{\perp}^{-3} for $k_{\perp} > k_S$ (not shown).

Comparing the saturation stage of precessing turbulence with other quasi-2D flows, the spectrum k_{\perp}^{-3} has been observed in “isotropically” forced rotating turbulence [23, 36, 39–41]

and in rapidly rotating Rayleigh-Bénard convection [24,42]. The observed spectrum is associated with an inverse energy cascade, as also observed in the present simulations for the saturation stage (see bottom inset of Fig. 3 and right inset of Fig. 4). For the atmosphere, which is viewed as a quasi-2D flow at large scales as the recent analysis of data with modern velocimetry techniques shows [25], both inertial scalings k^{-3} and $k^{-5/3}$ are observed in measured kinetic energy spectra [43]. However, these spectra give no indication of whether the turbulent flux $\Pi(k,t) = \int_k^\infty T(k')dk'$ within their associated range of scales is a direct (3D) or inverse (2D) energy flux in the atmosphere which would display a two-directional split energy cascade: part of the energy goes toward small scales (as in 3D) and part to large scales (as in pure 2D flows) [44,45]. Thus, results by [43] can be interpreted in terms of latitude-dependent scaling using the model by [38].

The similarity between the saturation stage dynamics and flows with strong rotation is also apparent from the development of the total energy spectrum $E(k) = \int_{S_k} e(\mathbf{k},t)dS_k$, i.e., the integral of the spectral energy density $e(\mathbf{k},t)$ over a 3D

sphere of radius k . Theoretical arguments for forced rapidly rotating flows suggest that for the intermediate wave numbers $k_f \ll k \ll k_\Omega$, where k_f denotes the forcing wave number, $E(k)$ behaves like [17,46,47]

$$E(k) = C_\Omega(\Omega D)^{1/2}k^{-2}, \quad (11)$$

with $C_\Omega = 1.22\text{--}1.87$ [46]. This scaling is also observed in a DNS study of a rotating turbulence under precessionlike perturbation generated by a change of the rotation axis at a fixed time instant [27]. In our present DNS as well, the saturation stage spectrum $E(k)$ exhibits a k^{-2} behavior with an intermediate range plateau ($k_S < k < k_\Omega$) of $C_\Omega = 1.87$ (see Fig. 4) and the behavior of the saturation stage turbulent flux $\langle \Pi(k) \rangle_t$ clearly indicates an inverse cascade of energy for $k < k_S$ and direct cascade for $k_S < k < k_\Omega$ (see left inset of Fig. 4).

This study identifies, through a careful analysis of energy spectra, the common features of the saturation stage resulting from the effects of nonlinear interaction on the precessional instability with other quasi-2D rotating flows.

-
- [1] F. Stefani, T. Albrecht, G. Gerbeth, A. Giesecke, T. Gundrum, J. Hérault, C. Nore, and C. Steglich, *Magnetohydrodynamics* **51**, 275 (2015).
- [2] W. V. R. Malkus, *Science* **160**, 259 (1968).
- [3] R. R. Kerswell, *J. Fluid Mech.* **321**, 335 (1996).
- [4] K. Glampedakis, N. Andersson, and D. I. Jones, *Mon. Not. R. Astron. Soc.* **394**, 1908 (2009).
- [5] R. R. Kerswell, *Geophys. Astrophys. Fluid Dynam.* **72**, 107 (1993).
- [6] A. Mahalov, *Phys. Fluids* **5**, 891 (1993).
- [7] H. Poincaré, *Bull. Astron. (Paris)* **27**, 321 (1910).
- [8] B. J. Bayly, *Phys. Rev. Lett.* **57**, 2160 (1986).
- [9] R. R. Kerswell, *Annu. Rev. Fluid Mech.* **34**, 83 (2002).
- [10] R. Lagrange, P. Meunier, F. Nadal, and C. Eloy, *J. Fluid Mech.* **666**, 104 (2011).
- [11] W. Mouhali, T. Lehner, J. Léorat, and R. Vitry, *Exp. Fluids* **53**, 1693 (2012).
- [12] Y. Lin, J. Noir, and A. Jackson, *Phys. Fluids* **26**, 046604 (2014).
- [13] J. Noir, P. Cardin, D. Jault, and J. P. Masson, *Geophys. J. Int.* **154**, 407 (2003).
- [14] S. Goto, A. Matsunaga, M. Fujiwara, M. Nishioka, S. Kida, M. Yamato, and S. Tsuda, *Phys. Fluids* **26**, 055107 (2014).
- [15] R. M. Mason and R. R. Kerswell, *J. Fluid Mech.* **471**, 71 (2002).
- [16] A. J. Barker, *Mon. Not. R. Astron. Soc.* **460**, 2339 (2016).
- [17] L. Biferale, F. Bonaccorso, I. M. Mazzitelli, M. A. T. van Hinsberg, A. S. Lanotte, S. Musacchio, P. Perlekar, and F. Toschi, *Phys. Rev. X* **6**, 041036 (2016).
- [18] F. S. Godeferd and F. Moisy, *Appl. Mech. Rev.* **67**, 030802 (2015).
- [19] C. Cambon, N. N. Mansour, and F. S. Godeferd, *Energy J. Fluid Mech.* **337**, 303 (1997).
- [20] A. Babin, A. Mahalov, and B. Nicolaenko, *Appl. Math. Lett.* **13**, 51 (2000).
- [21] Q. Chen, S. Chen, G. L. Eyink, and D. D. Holm, *J. Fluid Mech.* **542**, 139 (2005).
- [22] M. Thiele and W.-C. Müller, *J. Fluid Mech.* **637**, 425 (2009).
- [23] L. Bourouiba, D. N. Straub, and M. L. Waite, *J. Fluid Mech.* **690**, 129 (2012).
- [24] A. M. Rubio, K. Julien, E. Knobloch, and Jeffrey B. Weiss, *Phys. Rev. Lett.* **112**, 144501 (2014).
- [25] P. Héas, E. Mémin, D. Heitz, and P. D. Mininni, *Tellus A* **64**, 10962 (2012).
- [26] J. F. Scott, *J. Fluid Mech.* **741**, 316 (2015).
- [27] K. P. Iyer, I. Mazzitelli, F. Bonaccorso, A. Pouquet, and L. Biferale, *Eur. Phys. J. E* **38**, 128 (2015).
- [28] J. Jiang, D. Kong, R. Zhu, and K. Zhang, *Phys. Rev. E* **92**, 033007 (2015).
- [29] A. Salhi and C. Cambon, *Phys. Rev. E* **79**, 036303 (2009).
- [30] C. C. Wu and P. H. Roberts, *Geophys. Astrophys. Fluid Dyn.* **103**, 467 (2009).
- [31] A. H. Nayfeh, *Introduction to Perturbation Techniques* (Wiley, New York, 1981).
- [32] L. Bourouiba and P. Bartello, *J. Fluid Mech.* **587**, 139 (2007).
- [33] G. Lesur and P.-Y. Longaretti, *Mon. Not. R. Astron. Soc.* **378**, 1471 (2007).
- [34] S. Chakraborty, *Europhys. Lett.* **79**, 14002 (2007).
- [35] O. Zeman, *Phys. Fluids* **6**, 3221 (1994).
- [36] A. Sen, P. D. Mininni, D. Rosenberg, and A. Pouquet, *Phys. Rev. E* **86**, 036319 (2012).
- [37] P. D. Mininni, D. Rosenberg, and A. Pouquet, *J. Fluid Mech.* **699**, 263 (2012).
- [38] S. Sukoriansky and B. Galperin, *J. Fluid Mech.* **805**, 384 (2016).
- [39] L. M. Smith, J. R. Chasnov, and F. Waleffe, *Phys. Rev. Lett.* **77**, 2467 (1996).
- [40] L. M. Smith and Y. Lee, *J. Fluid Mech.* **535**, 111 (2005).
- [41] A. Pouquet, A. Sen, D. Rosenberg, P. D. Mininni, and J. Baerenzung, *Phys. Scr.* **2013**, 014032 (2013).
- [42] K. Julien, A. Rubio, I. Grooms, and E. Knobloch, *Geophys. Astrophys. Fluid Dyn.* **106**, 392 (2012).
- [43] G. Nastrom, W. Jasperson, and K. Gage, *Nature (London)* **310**, 36 (1984).
- [44] D. Byrne and J. A. Zhang, *Geophys. Res. Lett.* **40**, 1439 (2013).
- [45] G. Sahoo, A. Alexakis, and L. Biferale, *Phys. Rev. Lett.* **118**, 164501 (2017).
- [46] Y. Zhou, *Phys. Fluids* **7**, 2092 (1995).
- [47] V. M. Canuto and M. S. Dubovikov, *Phys. Fluids* **9**, 2132 (1997).